A THREE-DIMENSIONAL TRANSIENT FINITE ELEMENT MODEL FOR TIG WELDING

by

P. Tekriwal, M. Stitt and J. Mazumder
Department of Mechanical and Industrial Engineering

A Report of the

MATERIALS ENGINEERING - MECHANICAL BEHAVIOR

College of Engineering, University of Illinois at Urbana-Champaign

August 1986

A THREE-DIMENSIONAL TRANSIENT FINITE ELEMENT MODEL FOR TIG WELDING

P. Tekriwal, M. Stitt, and J. Mazumder
Department of Mechanical and Industrial Engineering
University of Illinois at Urbana-Champaign
1206 West Green Street
Urbana, IL 61801

ABSTRACT

A three-dimensional mathematical model has been developed for arc welding processes. The model has been used to simulate TIG (Tungsten Inert Gas) welding process and can be extended for MIG welding process also. While the temperature profile show the same trend as reported in literature, close agreements have been found between the numerically estimated and the experimentally observed results for the aspect ratios of the stainless steel weld bead. Cooling rate predictions in different regions of the melt pool qualitatively agree with the dendrite arm spacing measurements. The region with high cooling rate has low dendrite arm spacing.

The finite element program ABAQUS has been used in order to obtain the numerical results. The formulation of the problem is described in detail and the subroutines that were used in conjunction with the ABAQUS program have been mentioned. These subroutines calculate the arc heat input, heat transfer coefficients at the integration point and generate a suitable mesh for the model.

LIST OF SYMBOLS

Cp	Specific heat of metal, J/Kg-K
Cp_{gas}	Specific heat of shielding gas, J/Kg-K
d	Weld depth, m
e	Exponential (= 2.7)
D	Nozzle diameter, m
h	Heat transfer coefficient, W/m^2-K
H	Latent heat of fusion for metal, J/Kg
k	Thermal conductivity of metal, W/m-K
k_{gas}	Thermal conductivity of shielding gas, W/m-K
$L(T)$	Differential operator
n	Iteration counter
$\underline{n}$	Unit vector normal to surface
N_i	Shape functions (i = 1,2,...8)
NPD	Nozzle-to-plate distance, m
Pr	Prandtl number of shielding gas
q''	Surface heat flux, W/m^2
q''_s	Specified heat flux on the surface, W/m^2
Re	Reynolds number of shielding gas flow
dS	Elemental surface area, m^2
t	Welding time, s
t^*	Dimensionless time, vt/x
Δt	Time step, s
T	Temperature of metal, K
T_a	Ambient temperature, K
T_i	Temperature at node i, K
T_L	Liquidus temperature of metal, K

T_S Solidus temperature of metal, K

u Internal energy, J/Kg

u_t Internal energy at time, t, J/Kg

v Welding speed, m/s

v_{gas} Shielding gas flow velocity, m/s

dV Elemental volume, m^3

w Weld width, m

x,y,z Physical coordinates, m

Greek Symbols

α Thermal diffusivity of metal, m^2/s

α_{gas} Thermal diffusivity of shielding gas, m^2/s

δ_{jk} Kronecker delta

$\partial/\partial t$ Partial derivative w.r.t. t, 1/s

$\underline{\nabla}$ $\underline{i} \, \partial/\partial x + \underline{j} \, \partial/\partial y + \underline{k} \, \partial/\partial z$, 1/m

$\overline{\varepsilon}$ Thermal emissivity

ε, η, ζ Natural coordinates, m

$\varepsilon_i, \eta_i, \zeta_i$ Natural coordinates of node i

η_{eff} Arc efficiency

ν_{gas} Kinematic viscosity of shielding gas, m^2/s

ρ Density of metal, Kg/m^3

ρ_{gas} Density of shielding gas, Kg/m^3

μ_{gas} Dynamic viscosity, Kg/m-s

σ Stefan-Boltzman constant = 5.6697×10^{-8} W/m^2-K

1. INTRODUCTION

Arc welding is one of the oldest and fastest growing metal joining processes which accounts for more than two thirds of the welding industry in terms of its equipment sale in the United States [1]. It has applications ranging from joining thin section pipelines to assembling most large metal structures such as bridges, farm equipment, cars, trains and nuclear reactors. And yet, the state-of-the-art has been developed mostly by experience rather than by understanding the science behind it. The difficulty has been due to the rather complex non-linear nature of heat flow in the process. It is only in the late 1930's that people started exploring the science of welding. Although, Wells [2] quotes Roberts as giving the solution for the heat dissipation due to conduction from a moving point source on an infinite sheet as early as 1923, usually the name of Rosenthal [3,4] is associated with the equation of the moving point source. Tall [5] quotes Boulton and Lance Martin [6] as developing the equation independently and simultaneously with Rosenthal in the mid 1930's. Since then quite a few analytical models have been suggested which one way or the other pertain to the Rosenthal equation and solution. Myers et al. [7] have summarized these analytical works and stated the simplifying assumptions which limit the use of these models.

With the advent of the computer age most of these assumptions are being eliminated and perhaps we can analyze now the heat flow in welding more accurately by computational mechanics than by conducting experiments which are likely to involve errors, not to mention the scarce technology available to measure very high temperatures. Nevertheless, experimental verification is necessary in order to develop confidence in the model. And such was the approach in the current model.

The aim of the continuing project under the auspices of the U.S. Army Construction Engineering Research Laboratory is to develop a complete generalized thermo-mechanical model for the arc welding process which, given the design requirements to meet the quality standards, can be used to optimize the process parameters. The first critical step was to select a method of analysis that would accommodate as many welding variables as possible and accurately predict the transient temperature profile. The temperature field plays a crucial role in determining the size of the melt-zone and the heat-affected-zone, the grain size and the microstructure, residual stresses and distortion, and thus overall quality of the weld.

A comprehensive literature survey was made to reach the conclusion that finite element technique is best suited for the job. It competes very well with finite difference methods in that the irregularly shaped material boundaries can be accurately represented in the formulation and hence finite element method is extensible to various welded structures. Also, after the thermal history has been calculated, the same finite element mesh can be used for stress analysis in order to determine residual stresses and distortions in the weld joint. A summary of analytical and numerical heat transfer models is given in Table 1 of M.S. thesis of Stitt [8].

Weld pool convection has been found to play significant role in the welding process. Woods and Milner [9] examined the effects of electromagnetic Lorentz forces and plasma jet surface shear forces on the weld pool. Heiple et al. [10] experimentally studied the effects of surface tension on the weld pool. Oreper and Szekely [11,12] determined the significance of the incident arc heat and electric current flux distributions on the weld pool convection. Chan et al. [13] have found the effect of surface tension to be more dominant at the surface of the weld pool than at the bottom. Kou and Wang

[14] determined the individual and combined effects of the buoyancy force, the electromagnetic force and the surface tension gradient. A positive surface tension gradient with respect to temperatures tends to make the weld pool deeper. While all of these studies have contributed to understanding welding more, a suitable model still does not exist to account for free surface in the weld pool convection in the transient analysis.

Although this model does not incorporate weld pool convection, yet due to incorporation of transient nature of the heat flow it is expected that the time-temperature history can be better understood compared to quasi-steady state models. This is also an ideal model to extend to MIG welding processes. Convection feature may be included in the finite element model at a future date.

The finite element package ABAQUS was successfully employed for the current TIG model. The numerical predictions have been successfully verified with experimentally observed physical dimensions of the melt-zone, the heat-affected-zone and dendrite arm spacing. This has led to confidence in the analysis with regard to modeling the arc heat input and checking the suitability of the ABAQUS package for the analysis. While many models have been given for TIG welding by the researchers, a suitable model for MIG welding is scarce. The current work provides a very good and reliable model for TIG welding and an extension work of the model to simulate MIG welding is in progress.

2. PHYSICS OF THE PROCESS

A welding arc having input heat flux distribution q" and moving in x-direction at a constant traverse speed v strikes the surface of the two plates that are to be welded (see Fig. 1). A constant flow of an inert gas, called the shielding gas, from the welding torch accompanies the arc to protect the weld from atmospheric contamination. As the arc proceeds along the weld centerline, much of the heat input is absorbed by the plates. As a result, heat flow is induced in all three dimensions causing the metal of the two plates to melt and join with each other on solidification later.

In order to model the process more accurately, it is important to note the following:

a. A part of the heat supplied by the arc is lost to the ambient surrounding the welding torch and the plates,

b. Heat is lost from the surface of the weld pool and the plates in the form of convection and radiation, and

c. The drift of the shielding gas coming directly onto the plate (a stagnation point flow situation when the torch is vertical) enhances the convective heat loss from the surface [15].

Assuming the Gaussian profile of the arc input heat flux distribution leads to symmetry about the weld centerline (x-axis) and this enables us to analyze only one of the two plates and thus reduce the cost of analysis considerably.

The model features the following process facts and idealizations:

1. It is an uncoupled heat conduction analysis. No stress analysis has been done.

2. Quite general convection and radiation boundary conditions are entertained.

3. Temperature dependence of material properties such as thermal conductivity and specific heat is allowed.

4. Latent heat of fusion is taken into account as an apparent increase in specific heat in the melting range of temperatures.

5. Vaporization of metal during the process is ignored.

6. There is no volumetric and internal heat generation in the process but the program can easily accommodate if one exists.

7. Heat flow is symmetric about the weld centerline (x-axis).

8. Radially symmetric Gaussian distribution of arc heat input is assumed.

9. Finite element program ABAQUS, along with a few modifying user subroutines, is employed to obtain the numerical results.

3. MATHEMATICAL FORMULATION

The appropriate energy equation without any internal heat generation is:

$$\rho C_p \frac{\partial T}{\partial t} = \underline{\nabla} \, (k \, \underline{\nabla} \, T) \tag{1}$$

Boundary conditions are given by the Fourier equation

$$\underline{q}'' = - k \, \underline{\nabla} \, T. \tag{2}$$

Heat flux q" consists of one or more of the following modes of heat transfer depending upon the boundary:

(i) $h \, (T - T_a)$, the convective heat loss;

(ii) $\overline{\epsilon}\sigma \, (T^4 - T_a^4)$, the radiative heat loss;

(iii) $-q_s''$, if the surface is receiving a specified heat flux, q_s''.

   q" = 0 on y = 0 - plane due to symmetry.

All other surfaces incur the heat losses due to convection and radiation and only the top surface (z = thickness) facing the torch receives heat flux from the arc.

The Galerkin method dictates

$$\int_V N_i \, L \, (T) \, dV = 0$$

or $$\int_V N_i \rho \, \dot{u} \, dV - \int_V N_i \, \underline{\nabla} \, (k \, \underline{\nabla} \, T) \, dV = 0 \tag{3}$$

$\dot{u} = C_p \, \partial T/\partial t$, $T = N_i \, T_i$ and N_i are shape functions.

Note that summation convention is assumed on repeated indices unless mentioned otherwise.

Eight-noded rectangular linear finite elements (Fig. 2) were used to discretize the plate. The shape functions are given by the equation $N_i = 1/8 (1 + \varepsilon\varepsilon_i)(1 + \eta\eta_i)(1 + \zeta\zeta_i)$, (no summation).

The highest order derivative that is allowable in Eq. (3) is one greater than the order of continuity in the interpolation equations. Since all the interpolation equations are of the order zero (continuity in T but not in the first derivative), derivatives greater than first order cannot appear in Eq. (3). This restriction can be avoided by reducing the order of L(T) using integration by parts, [16, p. 346].

Integrating the second term of Eq. (3) by parts

$$\int_V N_i \, \rho \, \dot{u} \, dV + \int_V \underline{\nabla} N_i \cdot k \, \underline{\nabla} T \, dV = \int_S N_i \, k \, \underline{\nabla} T \cdot \underline{n} \, dS. \qquad (4)$$

Substituting Eq. (2) and replacing $T = N_k T_k$.

$$\int_V N_i \, \rho \, \dot{u} \, dV + \int_V \underline{\nabla} N_i \cdot k \, \underline{\nabla} N_k \, dV \, T_k + \int_S N_i \, \underline{q}'' \cdot \underline{n} \, dS \qquad (5)$$

The time derivative of the internal energy term is taken by using the backward Euler's formula.

$$u_{t + \Delta t} = u_t + \frac{\partial u}{\partial t}\bigg|_{t+\Delta t} \Delta t$$

i.e., $\dot{u} = \dfrac{\partial u}{\partial t}\bigg|_{t+\Delta t} = \dfrac{u_{t + \Delta t} - u_t}{\Delta t}$ \qquad (6)

This method is unconditionally stable and is very sensitive to the grid size and the time step used [16]. Oscillations may occur in the numerical

values even though the method itself is stable. The amount of oscillation is dependent on the material properties, the size of elements, and the time step. Reductions of the element size in high temperature gradient regions and reduced time steps decrease the seriousness of oscillations. But elements that are too small will result in too many degrees of freedom raising the cost of numerical analysis. This fact motivated us to use an exponentially expanding grid in y- and z- directions and use small elements near the weld centerline (Fig. 3).

Substitution of Eq. (6) in Eq. (5) yields

$$\frac{1}{\Delta t} \int_V N_i \, \rho \, (u_{t+\Delta t} - u_t) \, dV + \int_V \underline{\nabla} N_i \cdot k \, \underline{\nabla} N_k \, dV \, T_k + \int_S N_i \, \underline{q}'' \cdot \underline{n} \, dS = 0$$

(7)

The non-linear system, Eq. (7), is linearized in the form

$$F_i \equiv K_{ij} T_j - b_i = 0 \tag{8}$$

and is solved by ABAQUS using a modified Newton method [28]. In the Newton method, the tangent matrix (the Jacobian matrix) is formed by differentiating F_i with respect to $T_j\big|_{t+\Delta t}$. That is,

$$K_{ij} = \frac{\partial F_i}{\partial T_j\big|_{t+\Delta t}} \tag{9}$$

F_i = left-hand side of Eq. (7).

The method is a modified Newton method because the Jacobian matrix K_{ij} is not formed exactly. We now describe how the Jacobian is formed.

Jacobian Contributions

The internal energy term gives

$$\frac{\partial}{\partial T_j}\bigg|_{t+\Delta t} \left[\frac{1}{\Delta t} \int_V N_i \, \rho \, (u_{t+\Delta t} - u_t) \, dV\right]$$

$$= \frac{1}{\Delta t} \int_V \rho \, C_p\bigg|_{t+\Delta t} \frac{\partial T}{\partial T_j} \, dV$$

$$= \frac{1}{\Delta t} \int_V N_i \, \rho \, C_p\bigg|_{t+\Delta t} N_j \, dV \tag{10}$$

$$C_p\bigg|_{t+\Delta t} = C_p(T_{t+\Delta t}), \text{ if } T_{t+\Delta t} < T_S \text{ or } T_{t+\Delta t} > T_L \, ;$$

$$= C_p + \frac{H}{T_L - T_S}, \text{ if } T_S < T_{t+\Delta t} < T_L.$$

This term is small outside the solidus-liquidus temperature range and is stiff inside that rather narrow range. This may result in a numerical instability. To avoid the problem, this term is modified to a secant term during early iterations of the solution to a time step [32].

Jacobian contribution of the conductivity term in Eq. (7) is:

$$\frac{\partial}{\partial T_j}\bigg|_{t+\Delta t} \left[T_k \int_V \underline{\nabla} N_i \cdot k \, \underline{\nabla} N_k \, dV\right]$$

$$= \delta_{jk} \int_V \underline{\nabla} N_i \cdot k \bigg|_{t+\Delta t} \underline{\nabla} N_k \, dV + T_k\bigg|_{t+\Delta t} \int_V \underline{\nabla} N_i \cdot \frac{\partial k}{\partial T}\bigg|_{t+\Delta t} N_j \underline{\nabla} N_k \, dV$$

$$= \int_V \underline{\nabla} N_i \cdot k \bigg|_{t+\Delta t} \underline{\nabla} N_j \, dV \tag{11}$$

$\partial k/\partial T$ is usually very small, that is thermal conductivity varies very slowly with temperature, and hence is neglected. Note that if the second term is not negligible, it will make the Jacobian matrix non-symmetric.

The boundary term contributions can be calculated as follows:

Note that $\underline{q}" \cdot \underline{n} \doteq h (T - T_a) + \overline{\epsilon\sigma} (T^4 - T_a^4) - q_s"$ ($\doteq$ sign has been used to mean that the equality stands with one or more terms on the right-hand side depending upon the boundary). The Jacobian contribution is

$$\frac{\partial}{\partial T_j}\Bigg|_{t+\Delta t} \int_S N_i \, \underline{q}" \cdot \underline{n} \, dS$$

$$= \int_S N_i \, \frac{\partial \underline{q}" \cdot \underline{n}}{\partial T}\Bigg|_{t+\Delta t} N_j \, dS$$

$$\doteq \int_S N_i \left[\frac{\partial h}{\partial T} (T - T_a) + h + 4\overline{\epsilon\sigma}T^3\right]_{t+\Delta t} N_j \, dS \qquad (12)$$

The modified Newton method then yields the following system:

$$C_j \left\{\frac{1}{\Delta t} \int_V N_i \rho \, C_p\Big|_{t+\Delta t} N_j \, dV + \int_V \underline{\nabla} N_i \cdot k\Big|_{t+\Delta t} \underline{\nabla} N_j \, dV\right.$$

$$\left. + \int_S N_i \left[\frac{\partial h}{\partial T} (T - T_a) + h + 4\overline{\epsilon\sigma}T^3\right]_{t+\Delta t} N_j \, dS\right\}$$

$$= -\frac{1}{\Delta t} \int_V N_i \rho (u_{t+\Delta t} - u_t) \, dV - \int_V \underline{\nabla} N_i \cdot k \, \underline{\nabla} N_j dV \, T_j - \int_S N_i \, q_n" \, dS \qquad (13)$$

where, $\quad T_j^{n+1}\Big|_{t+\Delta t} = T_j^{n}\Big|_{t+\Delta t} + C_j \qquad (14)$

$$(q_n" = \underline{q}" \cdot \underline{n})$$

4. METHOD OF SOLUTION

ABAQUS uses a front wave solver to solve the system of equations. This front wave technique uses Gaussian elimination in a sophisticated and efficient manner. The full global matrix is never stored at any time. The process alternates between the assembly of element coefficients and elimination of variables (solution). The technique is thoroughly described in [17,18].

Arc Heat Input Model

Modeling the heat input from the arc is the most critical task for it directly influences the temperature profile, and hence the cooling rates, and the size of the melt-zone and the heat-affected-zone [19]. The heat input from the arc to the plate is assumed to have a radially symmetric Gaussian distribution profile at any instant of time [20-23]. Smartt, et al. [24] also found their experimental data for heat flux to fit a form of circular Gaussian distribution.

$$q''(r) = q_0'' \, e^{-3r^2/r_b^2}$$

$$q''(x, y, t) = \frac{3\eta_{eff} \, VI}{\pi r_b^2} \, e^{-\frac{3}{r_b^2}[(x - vt)^2 + y^2]} \qquad (15)$$

where q'' = heat flux per unit area per unit time deposited on the plate, q_0'' = maximum q'' (at $r = 0$), r = distance from the center of the arc, r_b = arc beam radius describing a region in which 95 percent of the total heat is deposited on the plate, V = arc voltage, and I = arc current.

The arc is assumed to be at origin at the start ($t = 0$). A value of $\eta_{eff} = 0.8$ was determined to be appropriate experimentally by Stitt [8].

A user subroutine DFLUX was incorporated in ABAQUS to simulate the above heat input from the arc.

Natural convection heat transfer occurs on all surfaces of the plates except the plane of symmetry (y = 0). But the area directly beneath the nozzle of the torch experiences forced convection due to flow of the shielding gas. Based on previous models [20,25], h = 10 W/m^{2}K was used for all the surfaces not influenced by the shielding gas and the following empirical relation initially suggested by Gardon and Cobonpue for air [15] and later modified by Steen for any gas [26] was used for a part of the top surface under the nozzle of the welding torch:

$$h = 13 \, Re^{1/2} \, Pr^{1/3} \, k_{gas}/NPD$$

$$\text{Reynolds number } Re = \frac{v_{gas} \times D \times \rho_{gas}}{\mu_{gas}}$$

$$\text{Prandtl number } Pr = \frac{v_{gas}}{\alpha_{gas}} = \frac{\mu_{gas} \, C_{p_{gas}}}{k_{gas}}$$

Program HCALC calculates Re and Pr based on the properties of the shielding gas. It then generates subroutine FILM which contains the expression for h. Subroutine FILM is compiled with the main program and calculates h for every integration point at a time step. DFLUX and FILM both transform the coordinate system to the moving arc and then calculate the heat flux and the heat transfer coefficient at any point appropriately. It may be noted that constant values of h are used for every point under the nozzle. There is no radial variation of h. The heat loss due to convection accounts for a very minor part (less than 5 percent) of the total heat involved in the process and hence a more accurate representation of h will not produce any difference in overall results [27].

Radiation heat losses are accounted from all the surfaces except the plane of symmetry ($y = 0$) by using the equation $q = \bar{\epsilon\sigma} \, (T^4 - T_a^4)$. The emissivity value 0.25 has been used for stainless steel [39].

Mesh Generation

Mesh generation plays a crucial role for accuracy and economy of numerical results. Very high temperature gradients near the weld centerline require finer elements in the region. Program NRATOR [8] is specially designed for a TIG butt weld mesh. This program takes the dimensions of the plate, number of elements desired in x-, y-, and z- directions, arc beam radius and number of nodes desired under the beam diameter as input and generates the nodes and their coordinates in an output file which is directly acceptable to ABAQUS as an input file. NRATOR generates the mesh in such a way that size of the elements increases exponentially in the y- and z-directions as they get far away from the weld-line (x-axis). This is essential for a lower cost of the numerical analysis. Also, fine size elements near the weldline do not sacrifice accuracy of the numerical results. Figure 3 shows the finite element mesh generated for the samples.

Since first-order 8-noded rectangular elements are quoted to produce better results for the problem involving latent heat effects [28], the same are chosen. These elements use a 2 x 2 x 2 rule for numerical integration with the quadrature points located at the corners of the element. This results in only the diagonal terms of the Jacobian matrix associated with the internal energy rate term. Higher order elements use regular Gaussian quadrature points and are preferred for smooth problems not involving latent heat effects.

Since element numbering and not the node numbering is important to minimize the front width of frontal solution technique [17], the surrounding elements are numbered close to each other so that the variables are eliminated as quickly as possible thus achieving further economy in the solution. Program ERATOR [8] was written in order to suitably number the elements and produce the output that fits the input format of ABAQUS.

Figures 4 and 5 show the temperature dependent property values of stainless steel that were used to obtain the numerical results.

5. EXPERIMENTAL PROCEDURE

Figure 6 sketches the experimental set up that was used to weld stainless steel samples cut from 3/8 in. x 2 in. bar stock. The welding torch was held fixed at a fixed distance above the workpiece and the constant speed of the table was controlled by an INTEL 8825 computer. Since the welding process was automatic, a high frequency unit was included in the circuit to initiate and stabilize the arc. This unit also initialized the shielding gas flow.

Welding was performed on different samples with various combinations (Table 2) of travel speed (5 to 40 mm/s), voltage (9 to 12 V) and currents (100 to 210 A). Care was taken that welding was started and finished on a sample during constant speed travel of the table and not during the acceleration or deceleration of the table at the start or stop of the motor driving the table or the workpiece. Table 1 shows the fixed data used for all the samples.

The important data that were measured from the samples were the following:

1. Width and depth of the melt-zone,

2. Width and depth of the heat-affected-zone, and

3. Photographs of the microstructures to determine the relative dendrite arm spacing in different regions of the weldment.

Estimation of the Beam Diameter

The arc beam diameter is very critical in determining the heat input distribution. Even though it is difficult to measure its value experimentally, a good estimate must be made if numerical results are to make sense. Experimental estimations for its values were made for each power input by initiating the arc for a quick pulse on a stationary sample and measuring the size of the

molten surface. These estimates were found to be 3 mm for 100 A to 180 A current range and 4 mm for currents 200 A and above.

Table 1 Constant Welding Parameters

PROCESS PARAMETER   VALUE

1. Sample Size

     Length   152.4 mm (6 in.)
     Width   50.08 mm (2 in.)
     Thickness   9.5 mm (3/8 in.)

2. Electrode Extension Length   4.76 mm (0.1875 in.)
    from Torch Nozzle

3. Nozzle-To-Plate Distance   4.76 mm

4. Arc Orientation Angle
    WRT Sample   90°

5. Shielding Gas Flow Rate   0.425 m^3/hr (15 ft^3/hr)

6. Electrode Geometry

    Diameter   2.38 mm (3/32 in.)

    Tip Shape   Tapered

6. RESULTS AND DISCUSSION

In order to check the reliability that this finite element model is approximating an actual TIG welding process, comparisons were made between the numerical predictions and the experimental measurements of the weld bead dimensions. xy-isotherms on the top surface of the plate and xz-isotherms at the weld centerline cross-section ($y = 0$, plane) were plotted. The isotherm corresponding to the melting point (1700°K) determined the width and the depth of the melt-pool-zone (the weld bead) in the above two plots, respectively. These numerically calculated values of the weld width and depth along with their experimental values are listed and compared in Table 2 for different samples.

The data of Table 2 can be pictorially viewed and compared in Figs. 7 and 8 where the aspect ratio of the melt-zone (width to depth ratio) has been plotted against the welding speed and the power input, respectively. These plots are the least square fits through the data points. Figure 7 shows a lower numerical prediction of the aspect ratio than the experimental values but the trend of increasing aspect ratio with increasing welding speed is the same in the numerical as well as the experimental curve.

Figure 8 shows that the numerical results are more accurate in the low power range than in the high power input range. This may be due to the inaccuracy involved in measuring the arc beam diameter at high power input. A more accurate understanding of the mechanism of heat flow from the arc to the plate is required for a better model. Including the weld pool convection effects might bridge the difference in the numerical and experimental results.

Table 2 Width and Depth Results for the Melt Zone

Sample	Net Power Input (W)	Arc Speed (mm/s)	Beam Diameter (mm)	NUMERICAL Width (mm)	Depth (mm)	EXPERIMENTAL Width (mm)	Depth (mm)	Error (%) Width	Depth
SS20	720	5	3	3.12	1.1	3.51	1.09	11.1	0.9
SS24	1280	20	4	3.04	0.952	2.96	0.95	2.7	0.2
SS27	1920	20	4	3.84	1.13	3.61	0.85	6.4	32.9
SS28	2016	40	4	2.80	0.884	2.16	0.56	29.6	57.8
SS30	1344	30	3	3.2	0.92	--	--	--	--

Metallurgical Effects of the Thermal Cycle on the HAZ and Weld Metal

The heat-affected-zone and the melt-zone metal experience changes in microstructure due to the welding thermal cycle. The HAZ is subject to the full thermal cycle and the solidified metal is exposed to the cooling portion of the cycle. The changes are mainly caused by the extreme high heating and cooling rates which normally occur in these regions. The metallurgical effects of the thermal cycle can be very complex and may result in unfavorable changes in material properties [33]. Since the quality of the weld is dependent upon the properties in these regions, it is important to understand the nature of microstructural changes in the HAZ and the melt-zone.

A mathematical model has the potential to predict microstructural changes based on calculations of the thermal cycle experienced by the material. Specifically, peak temperature and cooling rate calculations can be used to predict the type of grain growth and final microstructure present in the weldment. Grains that form during solidification of the weld pool are nucleated by the solid crystals at the solid/liquid interface. The mode of grain growth is epitaxial [33], in which each grain forms as a continuation of one of the

grains along the fusion boundary. The grains grow in a columnar fashion as the fusion boundary propagates forward [33].

The grain size of the weld metal is determined by the grain size of the solid metal at the fusion boundary of the HAZ. The HAZ grain size is primarily determined by the peak temperature and the cooling rate to which it is exposed. In general, grain size decreases with increase in cooling rate [33-36]. Large cooling rates result in very fine grain distributions. The main location of interest is at the fusion boundary because the grain size in this region determines grain size in the weld metal. However, at the interface, the peak temperature is the melting point. Therefore, the most significant variable in determining grain size is the cooling rate.

Arc deposits are characterized by columnar grains. Because of the high cooling rates, these grains normally exhibit very fine dendritic textures. It is important to distinguish between grains and dendrites. The grains are single crystals of iron-rich solid solution, within which the alloying elements are heterogeneously mixed to form the much finer dendritic pattern [35]. Dendrites are continuous to some extent, even though secondary phases are precipitated along the interdendritic regions. Thus, when discussing grain size and structure, we are referring to the distribution of dendrites throughout the crystal. The dendritic pattern is very fine for high cooling rates. Likewise, lower cooling rates induce a coarser dendritic distribution in the grain.

Numerical Predictions of Grain Size and Distribution

Because grain growth in the weld metal is a function of cooling rate, numerical calculations of the cooling rate at the solid/liquid interface were performed. Cooling rates along the centerline of the weld metal were also

computed (see Figs. 9 and 10). Based on these calculations, the relative grain size at various locations of the weld cross-section can be predicted. The goal of this analysis was to evaluate the accuracy of the numerical model by comparing numerical predictions to experimentally measured results. A finer grain distribution is predicted at locations experiencing higher temperature gradients. Therefore, three different locations on the weld cross-section were chosen to compare results. The cooling rates at each position were calculated. To verify these calculations, photomicrographs of the grain distribution were taken at each location. The accuracy of the model can be checked by comparing the grain structure at each location. The location experiencing the lowest cooling rate should have the coarsest grain structure. Likewise, the distribution becomes finer with increasing cooling rates. The following sections present the results of the comparisons for two cases. In general, the predicted grain structure at each location followed the trends established by cooling rates.

Results of Grain Size/Cooling Rate Comparisons

Stainless steel samples with arc velocities of 5 and 40 mm/s (SS20 and SS28 respectively) were used to compare experimental and numerical results. Comparisons were made at three locations in the cross section. The locations chosen are shown in Fig. 11 and include the centerline surface, centerline bottom and surface edge of the cross-section. These positions provide the widest range of cooling rate data for each cross-section. A high magnification micrograph from a scanning electron microscope (SEM) was taken for each location. From these micrographs, the light colored primary dendrite arms can be seen. The dendrites are the primary austenite which formed during solidification. The discontinuous, dark colored phase is believed to be

residual δ-ferrite after the δ-γ phase transformation [37]. This phase forms during the last stages of solidification.

Slow Welding Speed Comparisons

Sample SS20 was performed with an arc velocity of 5 mm/s. Cooling rate variations with position (y,z) increase with increase in the welding speed. Therefore, large differences in cooling rates within the cross-section were not expected for this velocity. Faster welding speeds allow less time for heat diffusion and result in greater temperature differences in the weld. Surface boundary conditions, combined with larger temperature differences produce larger cooling rate differences for faster speeds. Figure 9 shows the interface cooling rates at various non-dimensional times, t^*. Cooling rates for the bottom center (position 0.0) and surface edge (position 1.0) are shown in this figure. The cooling rate for the surface center is plotted in Fig. 10. Figure 9 reveals that the cooling rates are approximately equal until the arc passes completely away from the cross-section. At this time, no more heat is directly absorbed at the surface and natural convection and radiation effects cause a more rapid decrease in temperature for surface locations. Therefore, at times greater than $t^* = 1.0$, the surface edge location cools faster than the remaining portion of the interface which is still subject to diffusion of heat energy from surrounding hotter areas. Figure 9 correctly depicts these trends. The plot also shows that the differences in cooling rates along the interface are small for slow traverse speeds.

Figure 10 shows the variation in cooling rates for surface centerline locations. As expected, this plot correctly shows that locations which experience the highest peak temperatures cool faster due to the dominance of

the quartic, Stephan-Boltzmann radiation at the surface: $q = \bar{\epsilon}\sigma(T^4 - T_a^4)$.
Thus, the surface centerline position (which experiences the highest peak
temperature) will cool at a faster rate than the surface edge position.
Similarly, the surface edge position will have higher cooling rates than the
center bottom position because the surface convection and radiation losses
outweigh conduction and weld pool convection at the interface for high
temperatures. Again, the model correctly predicts these trends as shown in
Fig. 10. The plot shows the initial large differences in surface cooling
rates. It also shows that these differences rapidly decrease in a short time
due to the slower welding speed.

Grain structure predictions can be made based on these results. The
locations of highest cooling rates should have the smallest distances between
dendrites [34-38]. Therefore, compared to the edge and bottom positions,
dendrite arm spacings of the surface centerline should be much shorter. Since
predicted cooling rates along the interface do not vary by a large amount, the
arm spacings for the edge and bottom should not differ significantly.

The experimental results for dendrite arm spacings for both welding
speeds are presented in Table 3. Figure 11 shows the overall weld cross-
section and the dendritic structure in the three observed locations. The
experimental results were obtained by measurements from high magnification
photographs of each position.

Table 3 Dendrite Arm Spacing Results

Sample	Surface Center	Bottom Center	Surface Edge
SS20	0.63 mm	0.65 mm	0.688 mm
SS28	0.584 mm	0.725 mm	0.62 mm

From Table 3, it can be concluded that the numerical cooling rate calculations predicted the correct trends in dendrite arm spacings. The interface dendrite spacings are very close because of the low differences in cooling rates. The average spacing at the centerline surface (0.63 mm) is the smallest measured spacing as expected. However, the bottom center measurement showed a slightly smaller spacing than the surface edge. Since these values were expected to be close, the errors involved in experimental measurements of the micrographs may explain this discrepancy.

Fast Welding Speed Comparisons

Sample SS28 was performed with an arc velocity of 40 mm/s. The net power input for this sample (2016 W) was also higher than the previous sample (720 W). The numerical results should show greater overall magnitudes of cooling rates and larger differences in cooling rates throughout the cross-section. The interaction time with the surface elements is shorter due to faster arc velocity. Therefore, less time is available for heat diffusion through the thickness before the arc is at another location. The higher power input causes larger surface peak temperatures. Initial cooling rates are therefore higher due to the quartic radiation loss. Thus, the expected results would be finer grain structures at each position and larger differences in sizes at the three observed locations in the cross-section.

Figure 12 plots the interface cooling rates for the higher velocity case. The same basic trends as discussed for the slow speed case are evident

here. However, the model predicts much larger differences between the surface edge and bottom center cooling rates as expected. This plot also shows the expected higher magnitudes at each location due to the faster welding speed and power input.

The surface centerline cooling rates for this sample are given by Fig. 13. Again, the same reasoning applies to these results. The model predicts higher magnitudes and differences in cooling rates. The mathematical model predicts the correct trends of results for varying arc velocity and power input.

Figure 14 shows the cross-section and the three magnified areas of interest for sample SS28. These high magnification micrographs show the difference in dendrite spacing and allow for experimental measurements to verify the model's results [34,36-38]. Photographs such as these were used to estimate the experimental results of Table 3 for sample SS28.

Based on Figs. 12 and 13, the experimental results should show the same variation in grain distribution as before. However, the larger cooling rates should produce smaller dendrite arm spacings at each location. From Table 3, smaller spacings were observed experimentally at the surface locations. Average measurements for the center bottom location showed a higher (0.725 mm) spacing than the slow speed case. However, this case did show higher differences in dendrite spacing at each location. The order of increase in spacing was also correct for this case with the bottom centerline having the largest spacings. Thus, experimental results also agree very well for the high speed simulation.

7. CONCLUSION

1. The model has the capability of predicting good estimates of weld bead dimensions of a stainless steel weld. Aspect ratios (w/d) predicted are in close agreemtns with experimental results.

2. Qualitative grain size predictions based on cooling rates in different parts of the weld pool have also been verified by a study of micrographs of some samples.

3. A parametric study to determine the effect of different welding variables is possible with the model and this is useful in optimizing the welding process.

4. The temperature results of the analysis can be used for a thermo-mechanical analysis of the weld in order to predict residual stresses and distortions in the weld.

5. This model can be extended to simulate a Metal Inert Gas (MIG) welding process in which addition of filler metal keeps the finite element mesh changing with time.

6. A better modeling of the arc heat input will result in improved accuracy.

ACKNOWLEDGMENT

REFERENCES

1. Cary, H. B., "Modern Welding Technology," Prentice Hall, Inc., 1979, p. 17.

2. Wells, A. A., "Heat Flow in Welding," Weld. J., Vol. 31, May 1952, pp. 263s-267s.

3. Rosenthal, D., "Mathematical Theory of Heat Distribution During Welding and Cutting," Weld. J., Vol. 20, May 1941, pp. 220s-234s.

4. Rosenthal, D., "The Theory of Moving Sources of Heat and its Applications to Metal Treatments," Trans. ASME, Vol. 68, 1946, pp. 849-866.

5. Tall, L., "Residal Stresses in Welded Plates--A Theoretical Study," Weld. J., Vol. 43, Jan. 1964, pp. 10s-23s.

6. Boulton, N. S., and Lance Martin, H. E., "Residual Stresses in Arc Welded Plates," Proc. Inst. Mech. Engrs., (London), Vol. 133, 1936, pp. 295-347.

7. Myers, P. S., Uyehara, O. A., and Borman G. L., "Fundamentals of Heat Flow in Welding," Weld. Research Council Bulletin, Vol. 123, July 1967.

8. Stitt, M. C., "Optimization of Arc Welding Processes using a Three-Dimensional Finite Element Model," M.S. Thesis, Department of Mech. and Indus. Engr., University of Illinois at Urbana-Champaign, 1983.

9. Woods, R. A., and Milner, D. R., "Motion in the Weld Pool in Arc Welding," Weld. J., April 1971, pp. 163s-173s.

10. Heiple, C. R., Roper, J. R., Stagner, R. T., and Aden, R. J., "Surface Active Element Effects on the Shape of GTA, Laser and Electron Beam Welds," Weld. J., March 1983, pp. 72s-77s.

11. Oreper, G. M., Eager, T. W., and Szekely, J., "Convection in Arc Weld Pools," Weld. J., Nov. 1983, pp. 307s-312s.

12. Oreper, G. M., and Szekely, J., "Heat- and Fluid-Flow Phenomena in Weld Pools," J. Fluid Mech., Vol. 147, Oct. 1984, pp. 53-79.

13. Chan, C., Mazumder, J., and Chen, M. M., "A Two-Dimensional Transient Model for Convection in Laser Melted Pools," Met. Trans., Vol. 15A, Dec. 1984, pp. 2175-2184.

14. Kou, S., and Wang, Y. H., "Weld Pool Convection and Its Effect," Weld. J., Vol. 65, March 1986, pp. 63s-70s.

15. Gardon, R., and Cobonpue, J., "Heat Transfer Between a Flat Plate and Jets of Air Impinging on It," Int. Heat Transfer Conf., Part II, 1961, pp. 454-460.

16. Segerlind, L. J., "Applied Finite Element Analysis," John Wiley & Sons, Inc., Ch. 11, p. 221.

17. Irons, B. M., "A Frontal Solution Program for Finite Element Analysis," Int. J. Num. Meth. Engr., Vol. 2, 1970, pp. 5-32.

18. Hinton, E., and Owen, D. R. J., "Finite Element Programming," New York Academic Press, 1977.

19. Friedman, E., "Finite Element Analysis of Arc Welding," DOE Research and Development Report, Jan. 1980, Bettis Atomic Power Laboratory, West Mifflin, PA 15122.

20. Friedman, E., and Glickstein, S. S., "An Investigation of the Thermal Response of Stationary Gas Tungsten Arc Welds," Weld. J., Vol. 55, Dec. 1976, pp. 408s-420s.

21. Friedman, E., "Analysis of Weld Puddle Distortion and Its Effect on Penetration," Weld. J., Vol. 57, June 1978, pp. 161s-166s.

22. Pavelic, V., Tanbakuchi, R., Uyehara, O. A., and Myers, P. S., "Experimental and Computed Temperature Histories in Gas Tungsten-Arc Welding of Thin Plates," Weld. J., Vol. 48, July, 1969, pp. 295s-305s.

23. Krutz, G. W., and Segerlind, L. J., "Finite Element Analysis of Welded Structure," Weld. J., Vol. 57, 1978, pp. 211s-216s.

24. Smartt, H. B., Stewart, J. A., and Einerson, C. J., "GTA Heat Input Distribution Measurements," American Weld Soc. 66th Annual Convention, Las Vegas, NV, May 1985.

25. Hibbit, H. D., and Marcal, P. V., "A Numerical, Thermo-Mechanical Model for the Welding and Subsequent Loading of a Fabricated Structure," Computers and Structures, Vol. 3, Sept. 1973, pp. 1145-1174.

26. Steen, W. M., Ph.D. Thesis, Imperical College, London, 1976.

27. Mazumder, J., and Tekriwal, P., "Optimization of Welding Processes using a Mathematical Model," Progress Report prepared for the U.S. Army Construction Engineering Research Laboratory, Dec. 1984.

28. Hibbitt, Karlsson, and Sorensen, "ABAQUS Theory and User's Manuals," Hibbitt, Karlsson, and Sorensen, Inc., Providence, R.I., 1982.

29. Adams, C. M., Jr., "Cooling Rates and Peak Temperatures in Fusion Welding," Weld. J., Vol. 37, 1958, pp. 210s-215s.

30. Glickstein, S. S., Friedman, E., and Yeniscavich, W., "Investigation of Alloy 600 Welding Parameters," Weld. J., Vol. 54, April 1975, pp. 113s-122s.

31. Paley, Z., and Hibbert, P. D., "Computation of Temperatures in Actual Weld Designs," Weld. J., Vol. 54, Nov. 1975, pp. 385s-392s.

32. Traub, J. F., "Iterative Methods for the Solution of Equations," Prentice-Hall, Inc., Englewood Cliffs, N. J., 1964.

33. Lancaster, J. F., "Metallurgy of Welding," 3rd Ed., George Allen and Unwin Ltd., 1980, pp. 19-73.

34. Paley, Z., Lynch, J. N., and Adams, C. M., Jr., "Heat Flow in Welding Heavy Steel Plate," Weld J., Vol. 43, Feb. 1964, pp. 71s-79s.

35. Brown, P. E., and Adams, C. M., Jr., "Fusion-Zone Structures and Properties in Aluminum Alloys," Weld. J., Vol. 39, Dec. 1960, pp. 520s-524s.

36. Montoya-Cruz, J. J., Kadalbal, R., Kattamis, T. Z., and Giamei, A. F., "Coarsening and Microsegregation during Solidification of Ni-Al-Cr Dendritic Monocrystals," Met. Trans., Vol. 13A, No. 7, July 1982, pp. 1153-1159.

37. Kou, S., and Le, Y., "The Effect of Quenching on the Solidification Structure and Transformation Behavior of Stainless Steel Welds," Met. Trans., Vol. 13A, No. 7, July 1982, pp. 1141-1152.

38. Brooks, J. A., Williams, J. C., and Thompson, A. W., "STEM Analysis of Primary Austenite Solidified Stainless Steel Welds," Met. Trans., Vol. 14A, No. 1, Jan. 1983, pp. 23-31.

39. Incropera, F. P., and DeWitt, D. P., "Fundamentals of Heat and Mass Transfer," Second Edition, John Wiley and Sons, 1985.

LIST OF FIGURES

Figure 14 Cross Section of Sample SS28 showing
         the Dendritic Grain Structure at
         Three Locations
         (a) Top Center
         (b) Top Edge
         (c) Bottom Center
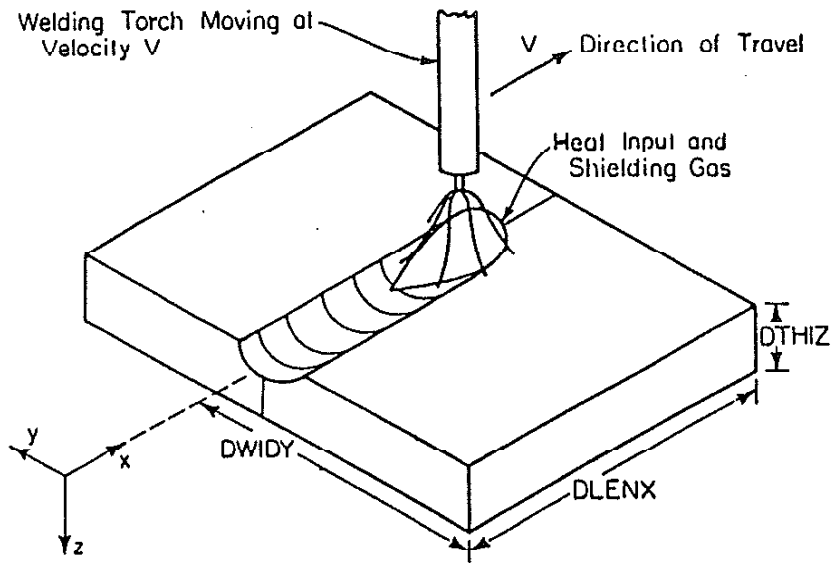
Figure 1   Illustration of TIG Arc Welding Process
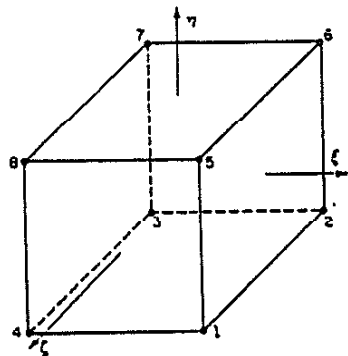
Figure 2   Basic Element with Local Coordinate System
and Local Node Numbering Sequence
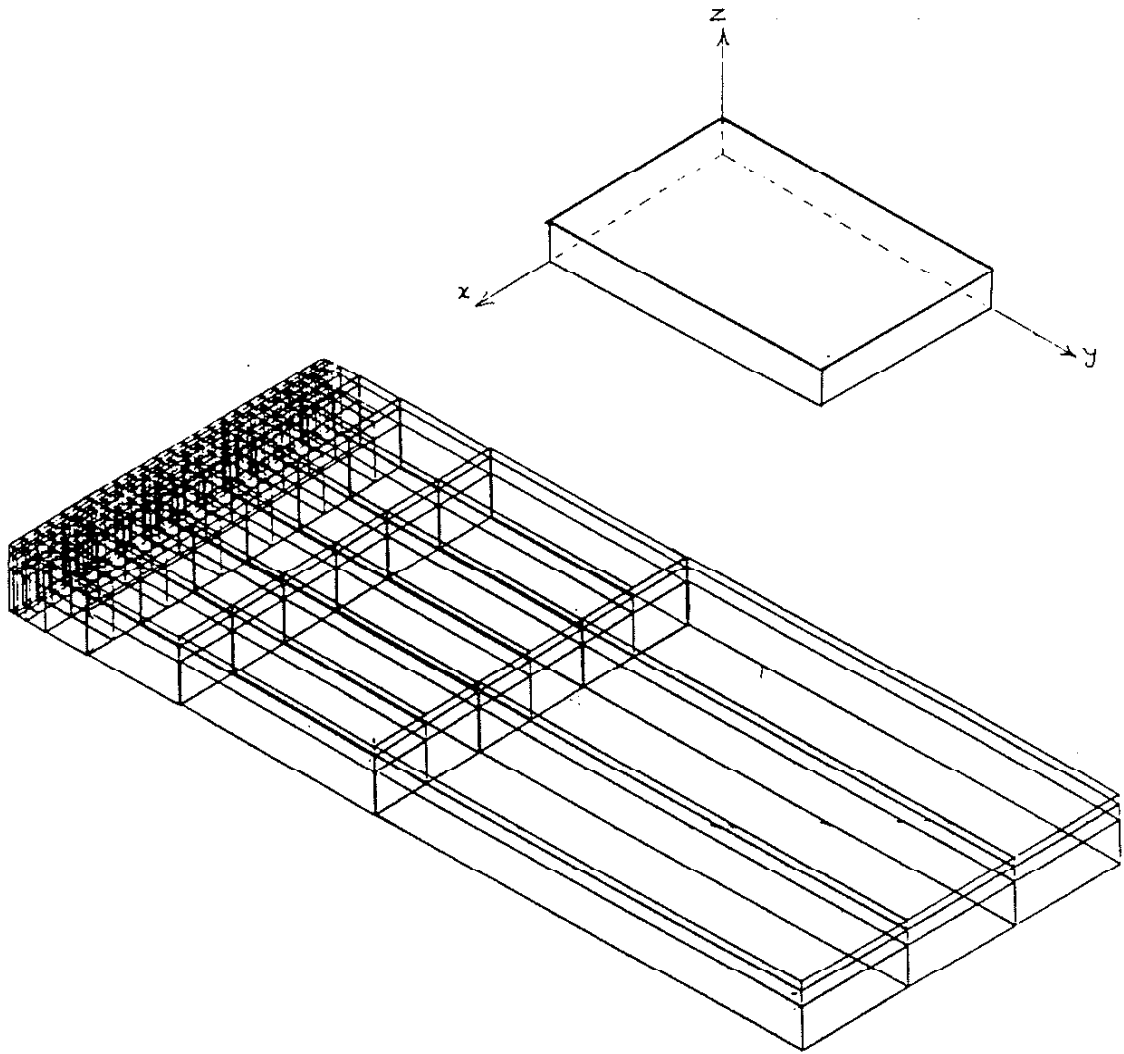
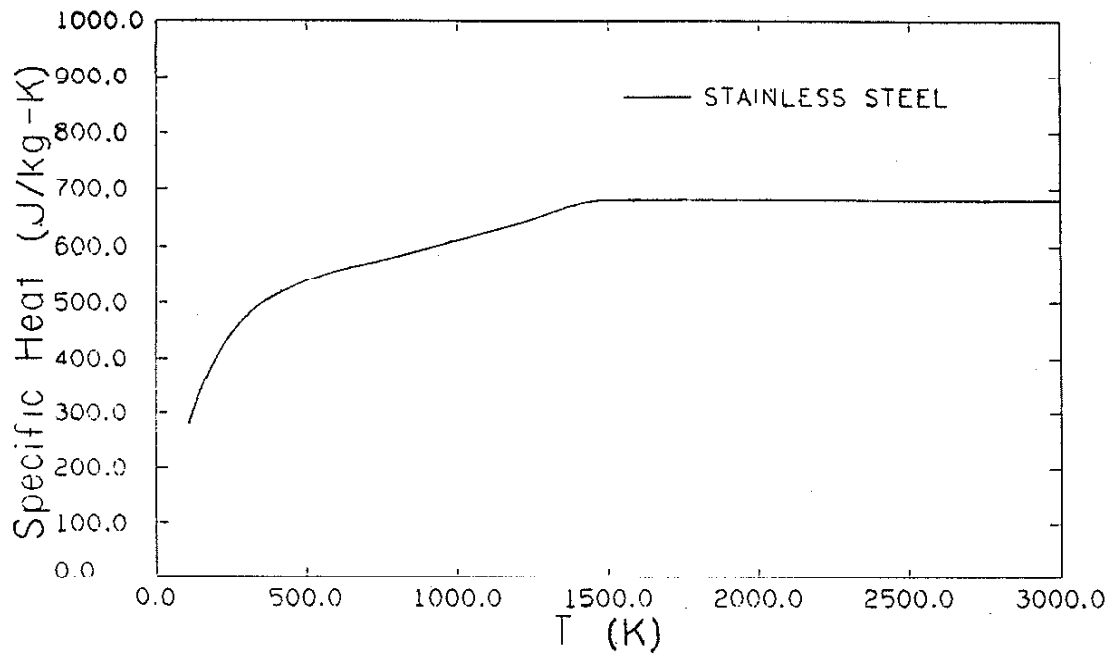Figure 3   TIG Butt-weld Mesh Used for Experimental Samples
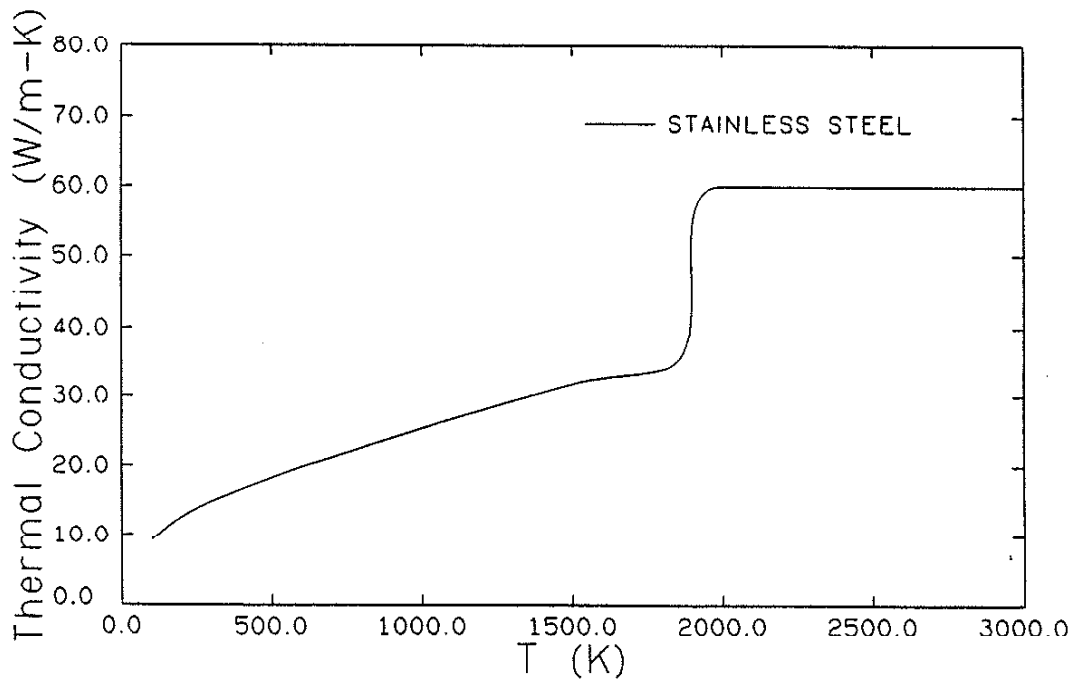
Figure 4   Specific Heat versus Temperature
for Stainless Steel Samples

Figure 5   Thermal Conductivity versus Temperature
for Stainless Steel Samples
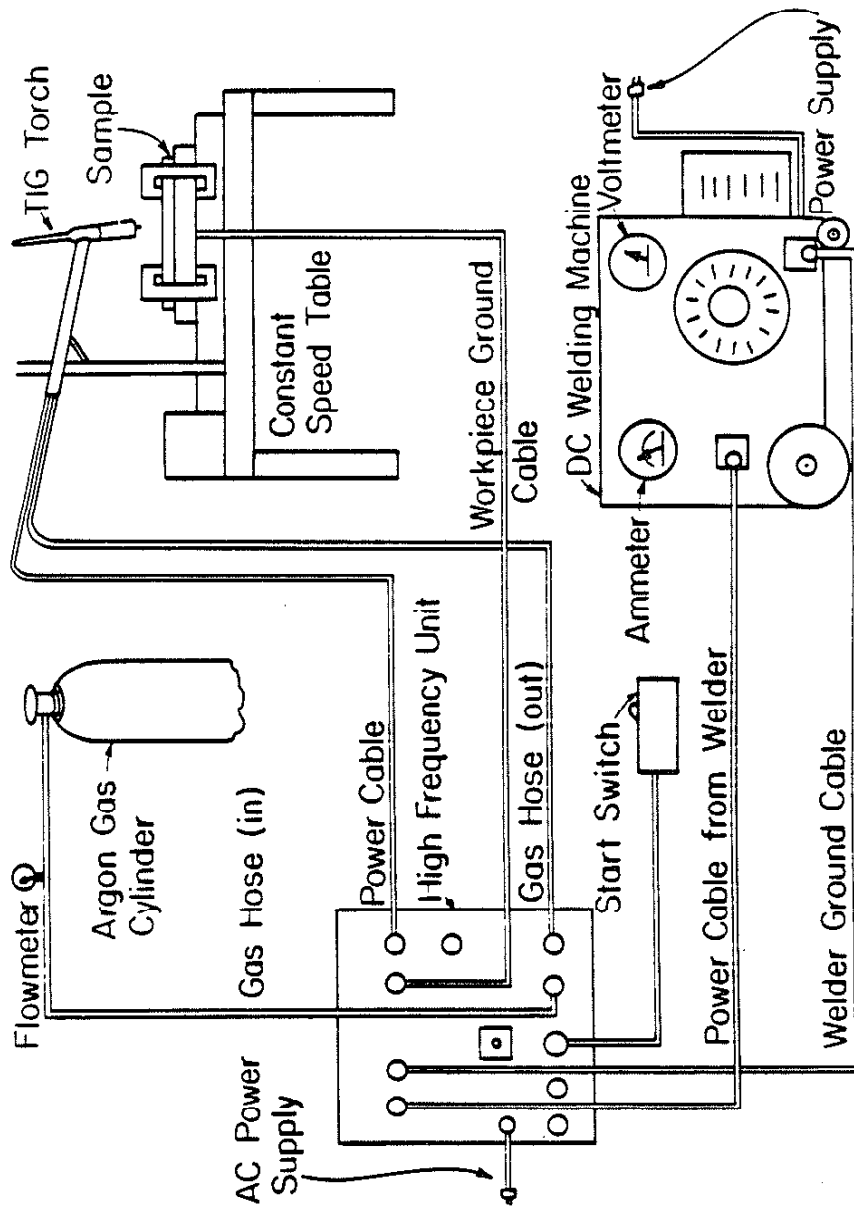
Figure 6   Experimental TIG Welding System
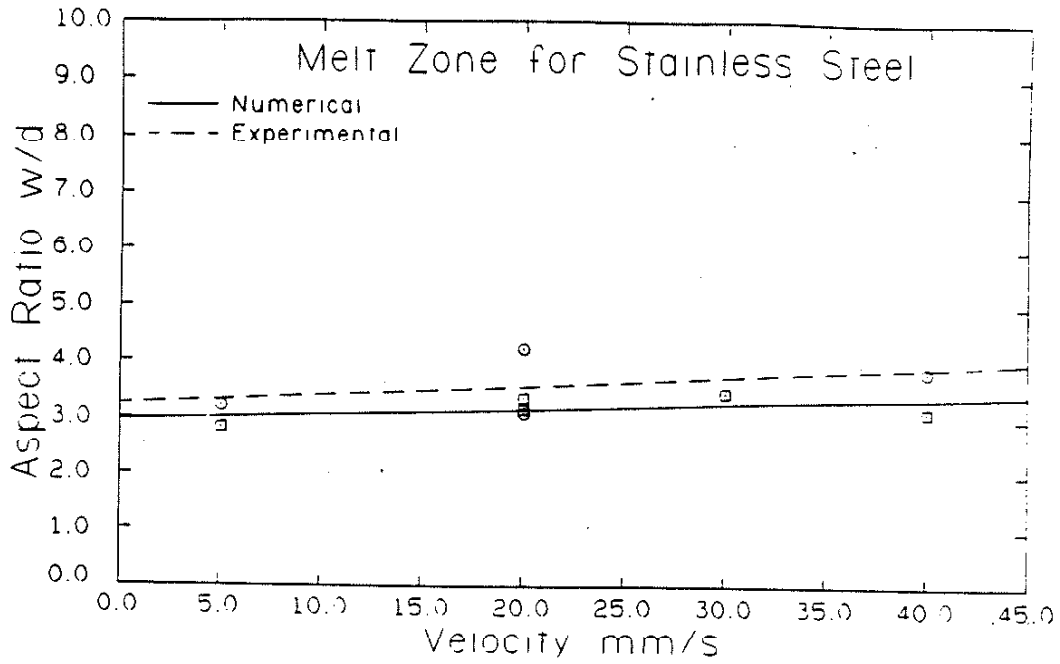
Figure 7 Aspect Ratio versus Velocity Data for the Melt Zone of Stainless Steel Samples
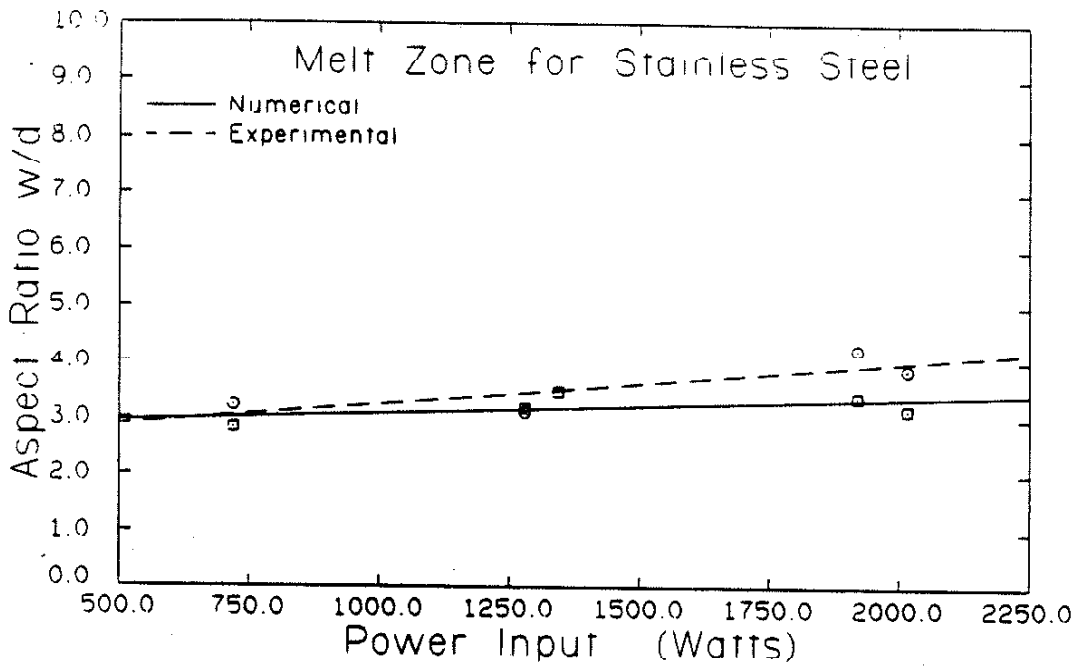
Figure 8 Aspect Ratio versus Power Input for the Melt Zone of Stainless Steel Samples
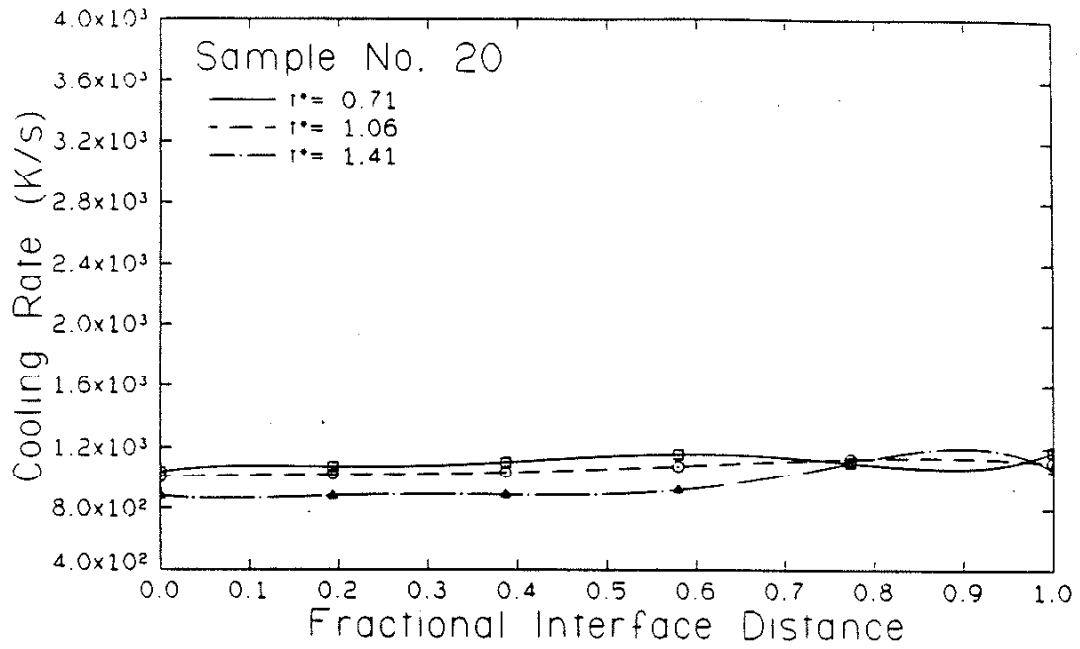
Figure 9 Cooling Rates along the Solid/Liquid Interface for Sample SS20
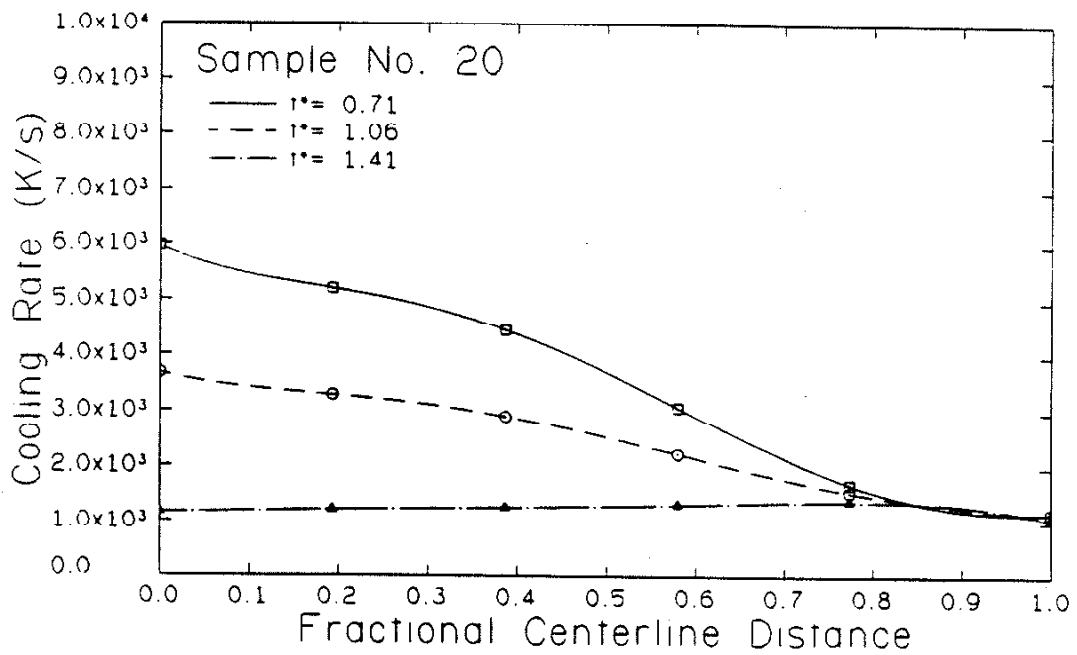
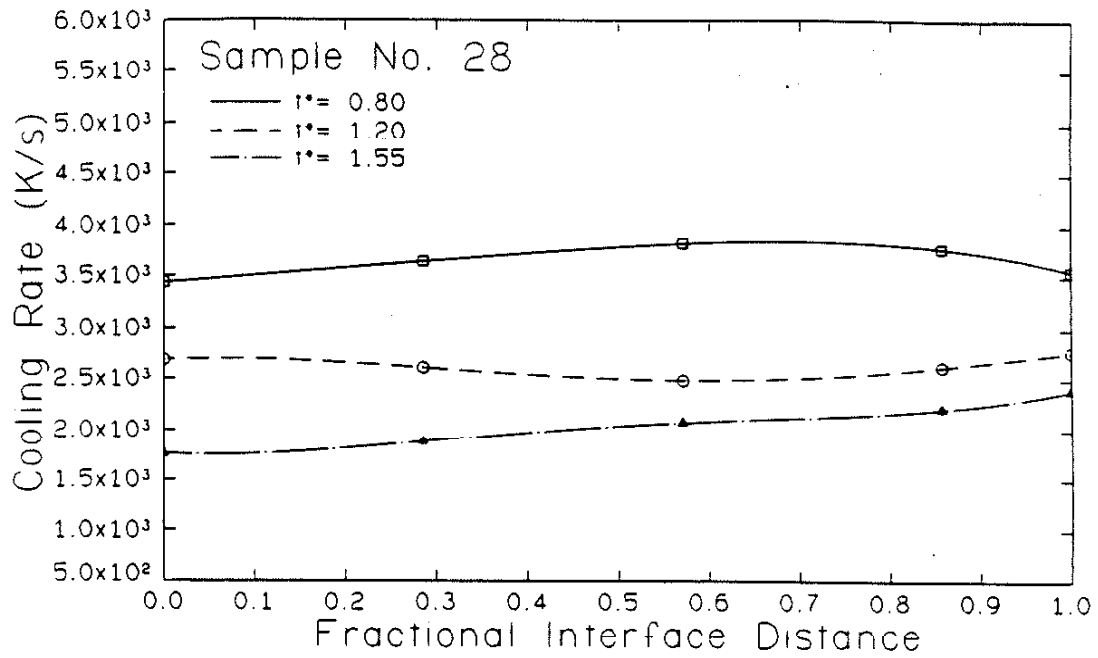**Figure 10 Cooling Rates along the Weld Centerline for Sample SS20**

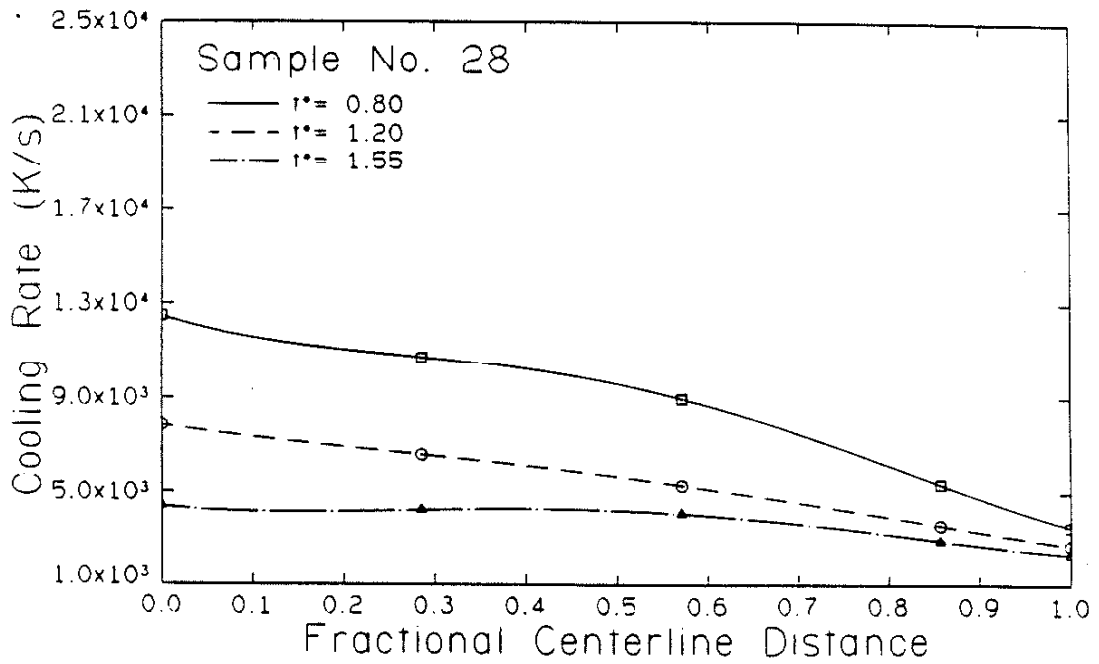Figure 12 Cooling Rates along the Solid/Liquid
Interface for Sample SS28

Figure 13 Cooling Rates along the Weld Centerline
for Sample SS28
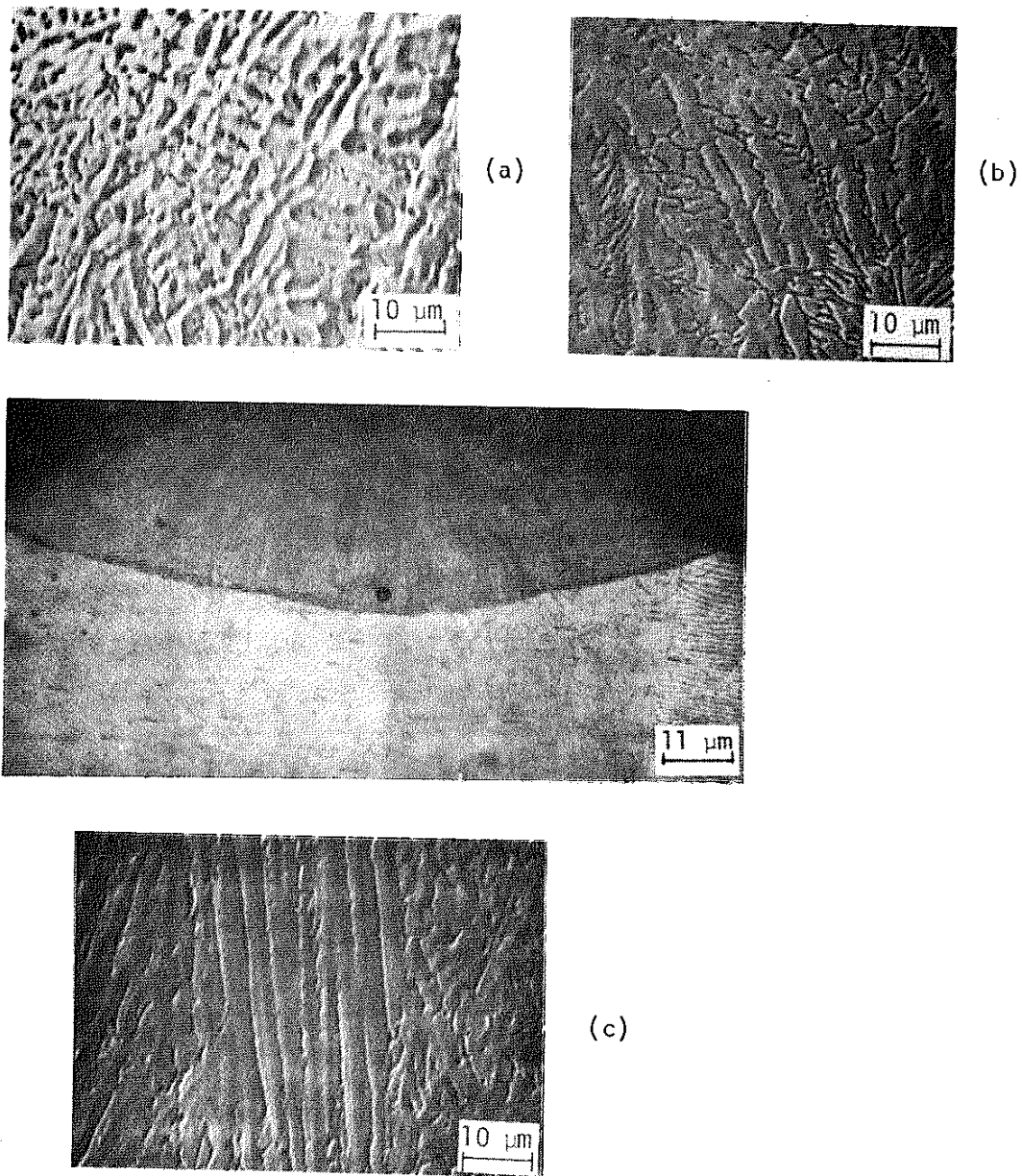
(a)

(b)

(c)

Fig. 14   Cross Section of Sample SS28 showing the Dendritic Grain
           Structure at Three Locations: (a) Top Center, (b) Top Edge,
           and (c) Bottom Center.